Rare Met. (2024) 43(7):3370–3382
https://doi.org/10.1007/s12598-024-02678-w

RARE METALS

ORIGINAL ARTICLE

Phase field modeling of grain stability of nanocrystalline alloys by explicitly incorporating mismatch strain

Min Zhou, Hong-Hui Wu*, Yuan Wu*, Hui Wang, Xiong-Jun Liu, Sui-He Jiang, Xiao-Bin Zhang, Zhao-Ping Lu*

Received: 6 September 2023 / Revised: 18 October 2023 / Accepted: 1 November 2023 / Published online: 16 April 2024

Abstract Nanocrystalline materials exhibit unique properties due to their extremely high grain boundary (GB) density. However, this high-density characteristic induces grain coarsening at elevated temperatures, thereby limiting the widespread application of nanocrystalline materials. Recent experimental observations revealed that GB segregation and second-phase pinning effectively hinder GB migration, thereby improving the stability of nanocrystalline materials. In this study, a modified phase-field model that integrates mismatch strain, solute segregation and precipitation was developed to evaluate the influence of lattice misfit on the thermal stability of nanocrystalline alloys. The simulation results indicated that introducing a suitable mismatch strain can effectively enhance the microstructural stability of nanocrystalline alloys. By synergizing precipitation with an appropriate lattice misfit, the formation of second-phase particles in the bulk grains can be suppressed, thereby facilitating solute segregation/precipitation at the GBs. This concentrated solute segregation and precipitation at the GBs effectively hinders grain migration, thereby preventing grain coarsening. These findings provide a new perspective on the design and regulation of nanocrystalline alloys with enhanced thermal stability.

Keywords Phase field model; Mismatch strain; Second-phase precipitation; Grain boundary segregation; Nanocrystalline alloys

M. Zhou, H.-H. Wu*, Y. Wu*, H. Wang, X.-J. Liu, S.-H. Jiang, X.-B. Zhang, Z.-P. Lu*
Beijing Advanced Innovation Center for Materials Genome Engineering, State Key Laboratory for Advanced Metals and Materials, University of Science and Technology Beijing, Beijing 100083, China
e-mail: wuhonghui@ustb.edu.cn

Y. Wu
e-mail: wuyuan@ustb.edu.cn

Z.-P. Lu
e-mail: luzp@ustb.edu.cn

H.-H. Wu
Institute for Carbon Neutrality, University of Science and Technology, Beijing 100083, China

H.-H. Wu, Y. Wu
Institute of Materials Intelligent Technology, Liaoning Academy of Materials, Shenyang 110004, China

1 Introduction

Nanocrystalline alloys with grain sizes <100 nm are widely recognized for their excellent mechanical properties [1–8]. Weertman et al. observed that the yield strength and total elongation of high-density, high-purity nanocrystalline Cu and Pd surpassed those of their coarse-grained counterparts [9]. However, the presence of numerous high-energy interfaces limits the application of these materials at elevated temperatures [2–4, 10–12]. Upon exposure to high temperatures, these tiny grains spontaneously merge, which triggers the coarsening of the nanocrystalline structure [1, 4]. Consequently, enhancing the thermal stability of nanocrystalline alloys is essential for controlling their high-temperature mechanical properties [13, 14].

To prevent excessive grain growth in nanocrystalline alloys, various strategies, such as second-phase particle pinning [15–17] and grain boundary (GB) segregation [18–21], have been employed to hinder GB migration. Moreover, the interactions among the solutes accumulated at the GBs resulted in concentration-dependent activation energy, reducing the GB energy and driving force for GB migration. Wang et al. [22] prepared nanocrystalline $(CoCrFeNi)_{93.5}Mn_{6.5}$ high-entropy alloy films with an average grain size of 25 nm via inert gas condensation.

Their results demonstrated that the dispersion of Cr-rich precipitates with body-centered cubic structures in the matrix effectively pinned GBs. Devaraj et al. [23] discovered that the coarsening resistance of nanocrystalline Al-Mg alloys during heating is attributed to the synergistic effect of the segregation of Mg at grain boundaries, which reduces the driving force for grain growth, and the formation of nanoscale Al_3Mg_2 precipitates pinning grain boundaries hinders grain boundary migration. Nevertheless, it is still challenging to comprehensively understand the competition between these multiple stabilization mechanisms and their synergistic effects on nanocrystalline materials by relying solely on experimental research.

Theoretical and computational methods are valuable for studying microstructural evolution, particularly those related to second-phase precipitation and solute segregation in nanocrystalline alloys [24–27]. Among these, the phase-field method, which is based on classical thermodynamics and kinetic theory, is frequently employed to simulate the phase transitions and evolution processes of material microstructures. This technique avoids the need to track the migration of phase interfaces during complex phase transformation processes [28–31] and is powerful for investigating the pinning effect of randomly distributed second-phase particles on the grain growth strain energy on solute segregation. As noted by Millett et al. [32], both the atomic size and solute concentration influence the GB energy. The results demonstrate that an increase in the atomic radius mismatch reduces the grain boundary energy. Furthermore, notably, the mismatch strain is inherently linked to atomic radius mismatch. However, the influence of the mismatch strain on the precipitation and segregation processes of nanocrystalline alloys has not been sufficiently considered by the phase-field model. Consequently, further research is required to explore the role of mismatched strains in these processes.

This study aims to develop a phase-field model of nanocrystalline alloys that incorporates mismatch strain to explore the influence of GB segregation and second-phase precipitation on grain growth. The competitive mechanism between these two events in terms of the average grain area distribution and resulting volume fraction was studied through statistical calculations and analysis. Based on these findings, an optimized strategy for tuning the grain stability of nanocrystalline materials was proposed. The improved model will be helpful in the development and refinement of nanocrystalline alloys with exceptionally high thermal stabilities for engineering applications.

2 Methods

2.1 Phase field model

In this study, the solute concentration field $c = c(\vec{r}, t)$ distinguishes the solvent from the solute, and the grains are denoted by the structural order parameter $\{\eta_i(\vec{r}, t), i = 1, ..., N\}$, where $\vec{r}$, t and N denote the position vector, time and number of order parameters required to describe the microstructure of the nanocrystalline alloys, respectively. Each order parameter represents a grain in the microstructure, and order parameters belonging to different grains cannot overlap [33]. For ease of understanding, the phase field variables are defined as $\vec{\eta} \equiv (\eta_1, \eta_2, ..., \eta_N)$. Consequently, the grains in the nanocrystalline system are described by $\vec{\eta} = (0, 0, ..., \eta_i = 1, ..., 0, 0)$, where $\vec{\eta} = (0, 0, ..., \eta_i = 1, ..., 0, 0)$ represents the GBs, and $0 < \eta_i, \eta_j < 1$. In particular, we expand the phase-field model of GB segregation to immiscible nanocrystalline alloys developed by Abdeljawad et al. [34, 35]. The total free energy F_{tot} comprises chemical energy F_{ch}, interface energy F_{int}, and elastic energy F_{el}, which are expressed as Eq. (1):

$$F_{tot} = F_{ch} + F_{int} + F_{el} \tag{1}$$

Here, the chemical free energy density f_{ch} is denoted as Eq. (2):

$$\begin{aligned} f_{ch} &= f(c, \eta_1, \eta_2, ..., \eta_N) = h(\vec{\eta}) f_{gb}\{c, T\} \\ &\quad + [1 - h(\vec{\eta})] f_b\{c, T\} + W_0 g(\vec{\eta}) \end{aligned} \tag{2}$$

where the free energies of the GB f_{gb} and bulk grain f_b depend on the solute concentration at a given temperature, T. $h(\vec{\eta})$ and $g(\vec{\eta})$ are both functions interpolating the free energy between GBs and the grains. According to the thermodynamic model of subregular solvents [36], f_{gb} and f_b can be expressed as Eq. (3):

$$\begin{aligned} f_\varphi &= G_\varphi^B c + G_\varphi^A (1 - c) + \frac{RT}{V_m}[c \ln c + (1 - c) \ln(1 - c)] \\ &\quad + \Omega_\varphi c(1 - c), \ \varphi = \text{gb,b} \end{aligned} \tag{3}$$

where the free energies of pure elements A and B are represented by G^A and G^B, respectively. The enthalpy of mixing is denoted as Ω_φ. The ideal gas constant is represented by R, and the molar volume is denoted by V_m.

At the center of the GB region, $h(\vec{\eta})$ is equal to 1, while within the grains, it is equal to 0. Recently, this interpolation function form was used to study the dynamics of grain growth in the presence of resistance at the three-phase junction [37]. The variable W_0 signifies the obstacle potential between the GB and bulk grain.

This study assumes that $h(\vec{\eta})$ share and $g(\vec{\eta})$ share the same functional form, represented by Eq. (4):

$$h(\vec{\eta}) = g(\vec{\eta}) = \frac{4}{3}\left[1 - 4\sum_{i=1}^{N} \eta_i^3 + 3\left(\sum_{i=1}^{N} \eta_i^2\right)^2\right] \tag{4}$$

The chemical free-energy density can be further simplified by combining Eq. (2) through Eq. (3), as Eq. (5):

$$f_{\mathrm{ch}} = f_{\mathrm{b}}\{c,T\} + \left\{W - a_1 c - a_2 c^2\right\} g\left(\overrightarrow{\eta}\right) \tag{5}$$

where W, a_1 and a_2 are expressed as Eq. (6):

$$\begin{aligned} W &= W_0 + \left(G_{\mathrm{gb}}^{\mathrm{A}} - G_{\mathrm{b}}^{\mathrm{A}}\right) \\ a_1 &= \left(G_{\mathrm{gb}}^{\mathrm{A}} - G_{\mathrm{b}}^{\mathrm{A}}\right) - \left(G_{\mathrm{gb}}^{\mathrm{B}} - G_{\mathrm{b}}^{\mathrm{B}}\right) - \left(\Omega_{\mathrm{gb}} - \Omega_{\mathrm{b}}\right) \\ a_2 &= \left(\Omega_{\mathrm{gb}} - \Omega_{\mathrm{b}}\right) \end{aligned} \tag{6}$$

Furthermore, the free energy density of the interface is defined as Eq. (7):

$$\begin{aligned} f_{\mathrm{int}} &= \frac{\kappa^2}{2}(\nabla c)^2 + \sum\nolimits_i^N \frac{\varepsilon^2}{2}|\nabla \eta_i|^2 \\ \nabla c &= \frac{\partial c}{\partial x} + \frac{\partial c}{\partial y} \end{aligned} \tag{7}$$

which represents the sum of the gradient energies between the phase boundaries and the GBs. In particular, κ and ε correspond to the gradient coefficients at the phase boundaries and GBs, respectively, and are correlated with their energies and interface widths.

F_{el} represents the elastic strain energy over the entire volume of the system, as represented by V, which can be expressed as Eq. (8) [38–40]:

$$F_{\mathrm{el}} = \frac{1}{2}\int_V \sigma_{ij}^{\mathrm{el}} \varepsilon_{ij}^{\mathrm{el}} \mathrm{d}V \tag{8}$$

where $\sigma_{ij}^{\mathrm{el}}$ and $\varepsilon_{ij}^{\mathrm{el}}$ are expressed by:

$$\varepsilon_{ij}^{\mathrm{el}} = \varepsilon_{ij} - \varepsilon_{ij}^0 + \varepsilon_{ij}^{\mathrm{ex}}, \tag{8a}$$

$$\varepsilon_{ij} = \frac{1}{2}\left(\frac{\partial u_i}{\partial x_j} + \frac{\partial u_j}{\partial x_i}\right) \tag{8b}$$

$$\varepsilon_{ij}^0 = \varepsilon_{00}\delta_{ij} f(c) \tag{8c}$$

$$\varepsilon_{00} = (1/a)(da/dc) \tag{8d}$$

$$f(c) = c^3\left(10 - 15c + 6c^2\right) \tag{8e}$$

where the elastic stress is represented by $\sigma_{ij}^{\mathrm{el}}$, and the elastic strain is represented by $\varepsilon_{ij}^{\mathrm{el}}$. In addition, $\varepsilon_{ij}^{\mathrm{el}}$ consists of the total strain ε_{ij}, intrinsic elastic strain ε_{ij}^0 and external strain $\varepsilon_{ij}^{\mathrm{ex}}$, as given by Eq. (8a). The expressions for ε_{ij} are given in Eq. (8b), where u_i and u_j are displacement field variables. ε_{ij}^0, defined in Eq. (8c), is related to the lattice-misfit ε_{00}, which is determined as the expansion coefficient calculated from the lattice parameter given by Eq. (8d). The Kronecker delta is represented by δ_{ij} such that its value equals 1 when $i = j$ and 0 when $i \neq j$ [41].

Considering the difference in the alternate elastic modulus between the matrix and the precipitate:

$$\sigma_{ij}^{\mathrm{el}} = C_{ijkl}\varepsilon_{ij}^{\mathrm{el}} \tag{9}$$

$$C_{ijkl} = f(c)C_{ijkl}^{\mathrm{P}} + (1 - f(c))C_{ijkl}^{\mathrm{M}} \tag{10}$$

where C_{ijkl} denotes the elastic modulus tensor. The elastic moduli of the precipitate and matrix are represented by C_{ijkl}^{P} and C_{ijkl}^{M}, respectively. According to Hooker's law, the elastic stress applied to a system can be expressed as Eq. (11):

$$\begin{aligned} \sigma_{ij} &= C_{ijkl}\varepsilon_{kl}^{\mathrm{el}} \\ &= \left[f(c)C_{ijkl}^{\mathrm{P}} + \left(1 - f(c)C_{ijkl}^{\mathrm{M}}\right)\left(\varepsilon_{kl} - \varepsilon_{kl}^0 + \varepsilon_{kl}^{\mathrm{ex}}\right)\right] \end{aligned} \tag{11}$$

Substituting Eq. (11) into Eq. (8), the elastic strain F_{el} is determined as follows:

$$\begin{aligned} F_{\mathrm{el}} &= \frac{1}{2}\int_V C_{ijkl}\varepsilon_{ij}^{\mathrm{el}}\varepsilon_{kl}^{\mathrm{el}}\mathrm{d}V \\ &= \frac{1}{2}\int_V \left[f(c)C_{ijkl}^{\mathrm{P}} + (1 - f(c))C_{ijkl}^{\mathrm{M}}\right]\left(\varepsilon_{kl} - \varepsilon_{kl}^0 + \varepsilon_{kl}^{\mathrm{ex}}\right)\left(\varepsilon_{ij} - \varepsilon_{ij}^0 + \varepsilon_{ij}^{\mathrm{ex}}\right)\mathrm{d}V \end{aligned} \tag{12}$$

The total free energy of the system was obtained by integrating the free energy density over the entire volume of the system, as represented by:

$$\begin{aligned} F_{\mathrm{tot}} &= F_{\mathrm{ch}} + F_{\mathrm{int}} + F_{\mathrm{el}} = \int_V \left(f_{\mathrm{ch}} + f_{\mathrm{int}} + f_{\mathrm{el}}\right)\mathrm{d}V \\ &= \int_V \left(f_{\mathrm{b}}\{c,T\} + \left(W - a_1 c - a_2 c^2\right)g\left(\overrightarrow{\eta}\right) + \frac{\kappa^2}{2}(\nabla c)^2 + \sum\nolimits_i^N |\nabla \eta_i|^2\right)\mathrm{d}V \\ &\quad + \frac{1}{2}\int_V \left(f(c)C_{ijkl}^{\mathrm{P}} + (1 - f(c))C_{ijkl}^{\mathrm{M}}\right)\left(\varepsilon_{kl} - \varepsilon_{kl}^0 + \varepsilon_{kl}^{\mathrm{ex}}\right)\left(\varepsilon_{ij} - \varepsilon_{ij}^0 + \varepsilon_{ij}^{\mathrm{ex}}\right)\mathrm{d}V \end{aligned} \tag{13}$$

The initial step of model exploration involves investigating how the enthalpy of mixing between the constituent elements and mismatch strain between the precipitate and matrix affect the GB free energy. For simplicity, we keep the free energy difference between the bulk grain and GB of both pure A and B equal, which implies that $\left(G_{\mathrm{gb}}^{\mathrm{A}} - G_{\mathrm{b}}^{\mathrm{A}}\right) = \left(G_{\mathrm{gb}}^{\mathrm{B}} - G_{\mathrm{b}}^{\mathrm{B}}\right)$, thus leading to $a_1 = -a_2 = -\left(\Omega_{\mathrm{gb}} - \Omega_{\mathrm{b}}\right)$.

In this study, we investigated four nanocrystalline systems with different lattice misfits, denoted by ε_{00} = 0, 0.02, 0.04 and 0.06 when Ω_{gb} = +0.05. The derivatives of the GB free energy can be described as $\frac{\partial^2 f_{\mathrm{tot}}(c)}{\partial c^2}$. According to the diffusion theory, when $\frac{\partial^2 f_{\mathrm{tot}}(c)}{\partial c^2}$ is less than 0, the chemical driving force is sufficient to enable the nucleation process to occur. Within this compositional interval, small perturbations in the chemical composition cause an increase in the Gibbs free energy, thus the system becomes metastable, which is conducive to the generation of nucleation sites [42]. Referring to the work of Wang et al. [43], a simplified function of the elastic energy can be written as $f_{\mathrm{el}}\prime(c) =$

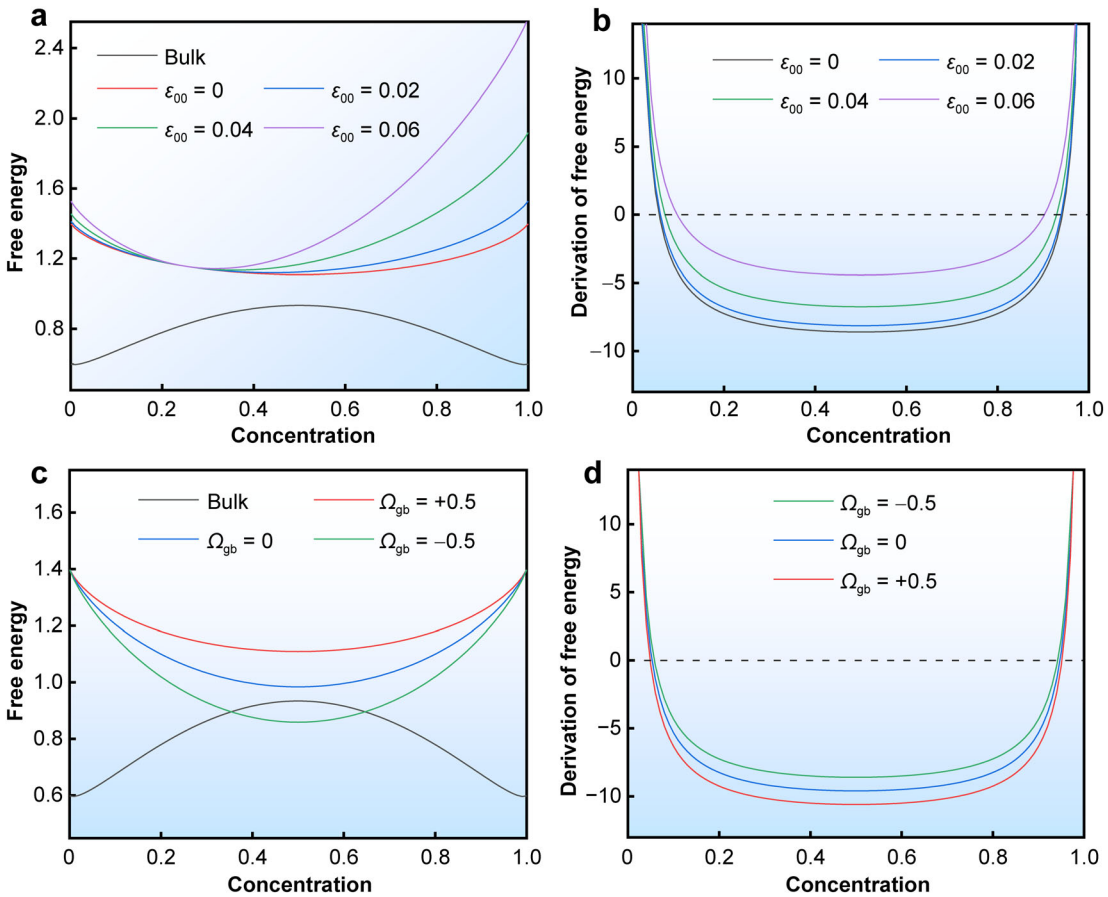

Fig. 1 Free-energy curves of bulk and GB systems **a** ε_{00} = 0, 0.02, 0.04, 0.06 and c Ω_{gb} = +0.5, 0 and −0.5; bulk thermodynamic parameters were assigned values of $G_b^A = G_b^B = RT/V_m$ = 0.6, Ω_b = 3.0, and W = 0.8. Derivation of GB free energy curves with different lattice misfits and enthalpy of mixing. **b** ε_{00} = 0, 0.02, 0.04, 0.06 and **d** Ω_{gb} = +0.5, 0 and −0.5

$\frac{V_m\varepsilon_{00}^2E}{1-v}(c-c_0)^2$ and $\frac{\partial^2 f_{el}\prime(c)}{\partial c^2}=\frac{2V_m\varepsilon_{00}^2E}{1-v}$. Based on the above definition, the simplified function of free energy is denoted as Eq. (14):

$$f'_{tot}(c) = f_b\{c,T\} + \{W - a_1c - a_2c^2\}g(\vec{\eta}) + \frac{V_m\varepsilon_{00}^2E}{1-v}(c-c_0)^2 + \frac{\kappa^2}{2}(\nabla c)^2 \quad (14)$$

where E is Young's modulus, and v is Poisson ratio.

Furthermore, after performing a second-derivative operation on the function, this term can be approximated as Eq. (15):

$$\frac{\partial^2 f'_{tot}(c)}{\partial c^2} = \frac{RT}{V_m}(1/c - 1/(1-c)) + (-2a_2)g(\vec{\eta}) + \frac{2V_m\varepsilon_{00}^2E}{1-v} \quad (15)$$

Figure 1a illustrates that the simplified free energy increases gradually as the mismatch strain increases. Figure 1b shows the derivative of the free energy shown in Fig. 1a. As the lattice misfit increases from 0 to 0.06, the bottoms of the curves shift towards the y = 0 guideline, resulting in a reduced region of spinodal decomposition. This indicates that increasing the mismatch strain makes the spontaneous nucleation process more challenging. Furthermore, we investigated three nanocrystalline systems with Ω_{gb} = −0.5, 0, +0.5 and ε_{00} = 0, as shown in Fig. 1c. As the value of Ω_{gb} decreased from positive to negative, a gradual decline in the GB free energy curve was observed, with its minimum point residing below the maximum value of the bulk curve. Similarly, Fig. 1d shows the plots of the derivatives of the GB free energy curves shown in Fig. 1c. Owing to the reduction in the GB mixing enthalpy parameters, the region of spinodal decomposition steadily decreased, rendering spontaneous nucleation increasingly difficult.

2.2 Kinetics and simulation conditions

The field variables evolve in time and space following the principle of energy dissipation in the system, as applied to the dynamic equations. The conserved field variable $c(\vec{r},t)$ is usually described by the Cahn-Hilliard diffusion equation alongside a noise term [42, 44], which takes the form:

Table 1 Normalized parameters used in present study

Simulation parameters	Values
Atomic mobility M	1.0
grain boundary mobility L	1.0-c_0
Gradient coefficient κ	1.0
Gradient coefficient ε	1.0
Obstacle energy scale W	0.8
Enthalpy of mixing in bulk Ω_b	3.0
Difference in free energy a_1	2.5
Difference in heat of mixing a_2	−2.5
Free energy of pure A in bulk G_b^A	0.6
Free energy of pure B in bulk G_b^B	0.6
Elastic modulus tensor of matrix G_{ij}^M	C_{11} = 603, C_{12} = 339, C_{44} = 304
Elastic modulus tensor of precipitate G_{ij}^P	C_{11} = 621, C_{12} = 323, C_{44} = 304

$$\frac{\partial c(\vec{r},t)}{\partial t} = \nabla M \nabla \frac{\delta F_{\text{tot}}}{\delta c(\vec{r},t)} + \xi(\vec{r},t) \tag{16}$$

For the nonconserved field variables, we used the relaxation equation, generally the Allen-Cahn type Eq. (17):

$$\frac{\partial \eta_N(\vec{r},t)}{\partial t} = L_N \frac{\delta F_{\text{tot}}}{\delta \eta_N(\vec{r},t)} + \zeta_N(\vec{r},t) \tag{17}$$

where M and L_N are the atomic and GB mobilities, respectively. ξ and ζ_N are noise terms, which are random numbers conforming to a Gaussian distribution and must interact to satisfy the fluctuation and dissipation theorems [45].

$$\langle \xi(\vec{r},t)\xi(\vec{r}\prime,t\prime)\rangle = -2k_B TM\nabla^2\delta(\vec{r}-\vec{r}\prime)\delta(t-t\prime) \tag{16a}$$

$$\langle \zeta_N(\vec{r},t)\zeta_N(\vec{r}\prime,t\prime)\rangle = -2k_B TL_N\nabla^2\delta(\vec{r}-\vec{r}\prime)\delta(t-t\prime) \tag{17a}$$

where k_B is the Boltzmann constant. $t\prime$ is a temporal variable. The noise term is closely related to the thermal fluctuation, which induces local fluctuations in the concentration and structural order parameter fields.

All the parameters used in this study were normalized [35] and listed in Table 1. The simulation area is a square with an area of $N_x = N_y$ = 100 nm, with each grid point being $\Delta x = \Delta y$ = 1.0 nm distance apart. In Sects. 3.1 and 3.2, c_0 = 0.25 was used as the uniform initial concentration, whereas in Sect. 3.3, four sets of concentrations, c_0 = 0.05, 0.10, 0.15 and 0.20, were selected to study the effects of the different solute concentrations. These values were chosen to represent the actual uniform initial distribution, thereby facilitating a more detailed analysis of the system behavior under different initial conditions.

3 Results and discussion

3.1 Effect of mismatch strain on precipitation in immiscible nanocrystalline alloys

Despite numerous experimental findings suggesting that the mismatch strain significantly impacts the precipitation behavior, tracing the effects of different lattice misfits on the precipitation process in real-time experimental states remains challenging. To investigate the role of the mismatch strain between the precipitate and matrix in the microstructural evolution and growth dynamics of the second phase during the phase transformation, four sets of lattice misfits were selected for analysis. Furthermore, the mixing enthalpy was set as positive with Ω_{gb} = +0.5, and c_0 = 0.25. As shown in Fig. 2a–d, under specific mismatch conditions, the solute concentration at the GBs gradually increased with aging time. The precipitates are shown in red, and those from the blue matrix are shown. Precipitates that reached the critical nucleus size (indicated in red) continued to expand, whereas smaller precipitates were either engulfed by larger surrounding particles or dissolved into the matrix.

However, as the lattice misfit increases from 0 to 0.06, the second-phase precipitation process is suppressed at an equivalent aging time, resulting in a reduced volume fraction and density of the precipitates. Figure 2a, b illustrates the microstructures of systems with lattice misfits of 0 and 0.02, respectively. As can be seen, the model with a lattice misfit of 0.02 contains nearly no secondary phase within its grain structure. Solute enrichment and precipitation at GBs effectively impede GB migration, hindering grain coarsening [15, 20]. As the lattice misfit increases to 0.04, the mismatch strain exerts a stronger inhibitory effect on the precipitation process over time. However, when the lattice misfit becomes excessively significant, the resulting increase in the elastic mismatch strain may increase the nucleation resistance of second-phase precipitation, leading to solute enrichment occurring solely at the GBs (Fig. 2d).

Statistical calculations based on ImageJ were conducted to analyze the distribution of the grain area in nanocrystalline alloys with varied lattice misfit strains at 200-time intervals. Precipitation was observed in areas where the concentration exceeds 0.8. In addition, the volume fraction of the precipitated phase (V_p) was measured over time. As shown in Fig. 3, the corresponding system exhibits a declining trend in the volume fraction of the precipitates as the lattice misfit increases. Particularly, in nanocrystalline

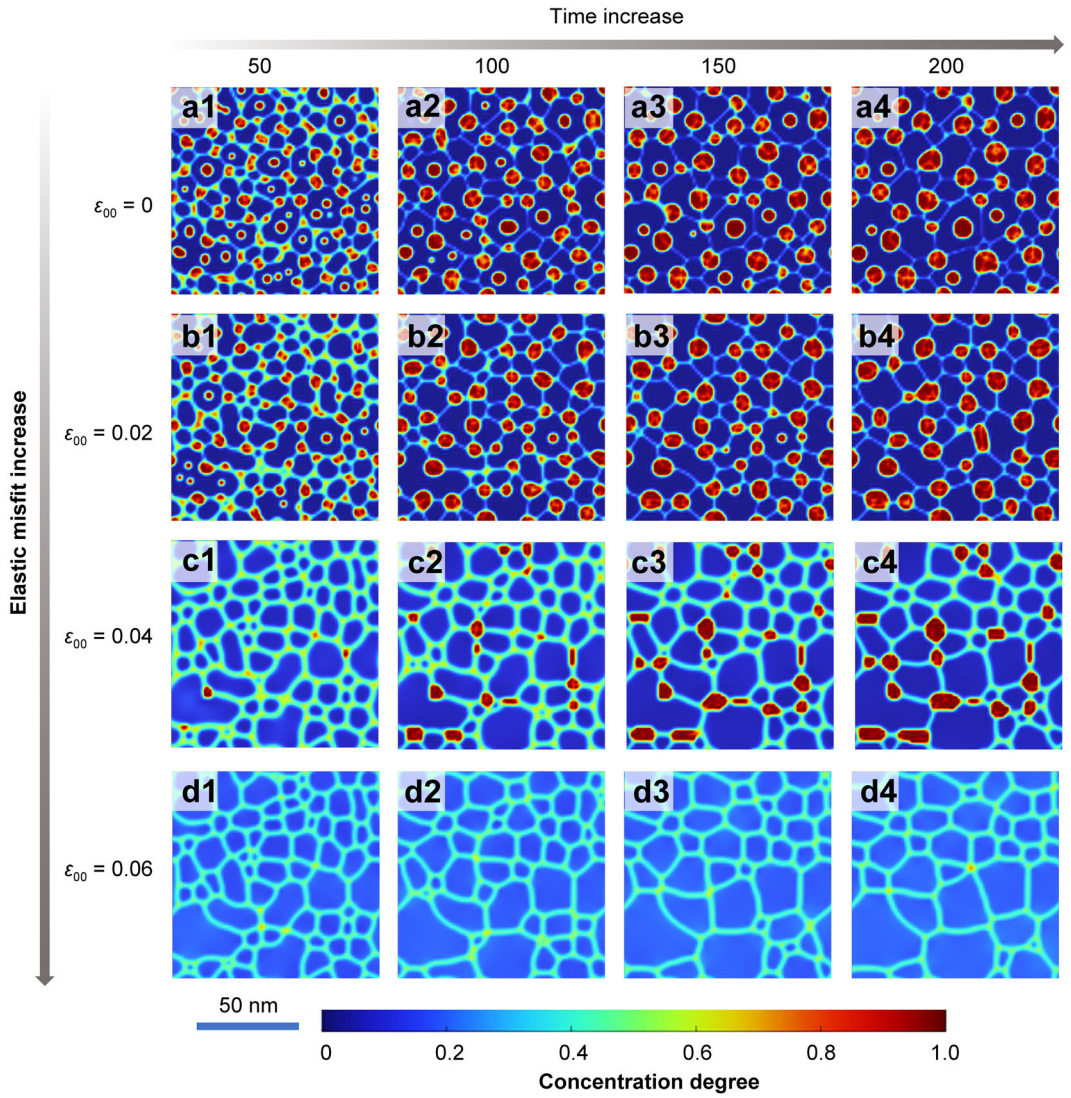

Fig. 2 Effect of lattice misfits **a** ε_{00} = 0, **b** ε_{00} = 0.02, **c** ε_{00} = 0.04 and **d** ε_{00} = 0.06 on microstructure evolution of second-phase precipitation in immiscible nanocrystalline alloys

alloys with a 0 lattice misfit, the grain area distribution ranged from 10 to 1375 nm^2. However, as the lattice misfit escalates to 0.02, the maximum grain size in the alloy significantly reduces from 1375 to 960 nm^2, resulting in a decrease in the fast-grown grains. This decrease primarily results from the substantial elastic effect that inhibits the precipitation of the secondary phase. The solutes in the alloy predominantly accumulated at the GBs, consequently impeding GB migration. Moreover, the grain size gradually increased from 960 to 1355 nm^2 as the lattice misfit increased to 0.06, resulting from the mismatch strain exerted on the precipitation at the GBs.

These findings indicate that as the lattice misfit increases, the particle volume fraction decreases. When the coupling mismatch strain is small, precipitation within the grains is effectively suppressed. However, when the mismatch strain becomes excessively large, the precipitation process of the second phase at the GBs is inhibited, resulting in a weakened pinning effect on grain boundary migration, thereby forming rapidly growing grains.

3.2 Effect of mismatch strain on precipitation in immiscible nanocrystalline alloys

Nanocrystalline materials possess structures characterized by loose GBs, which render them favorable for rapid atom (ion) diffusion and susceptibility to impurity atom (ion) segregation. The disordered alignment of atoms along the GBs results in several defects, such as vacancies and dislocations. These imperfections increase the boundary energy, causing the Gibbs free energy of GBs to exceed that of a single crystal with the same atomic component.

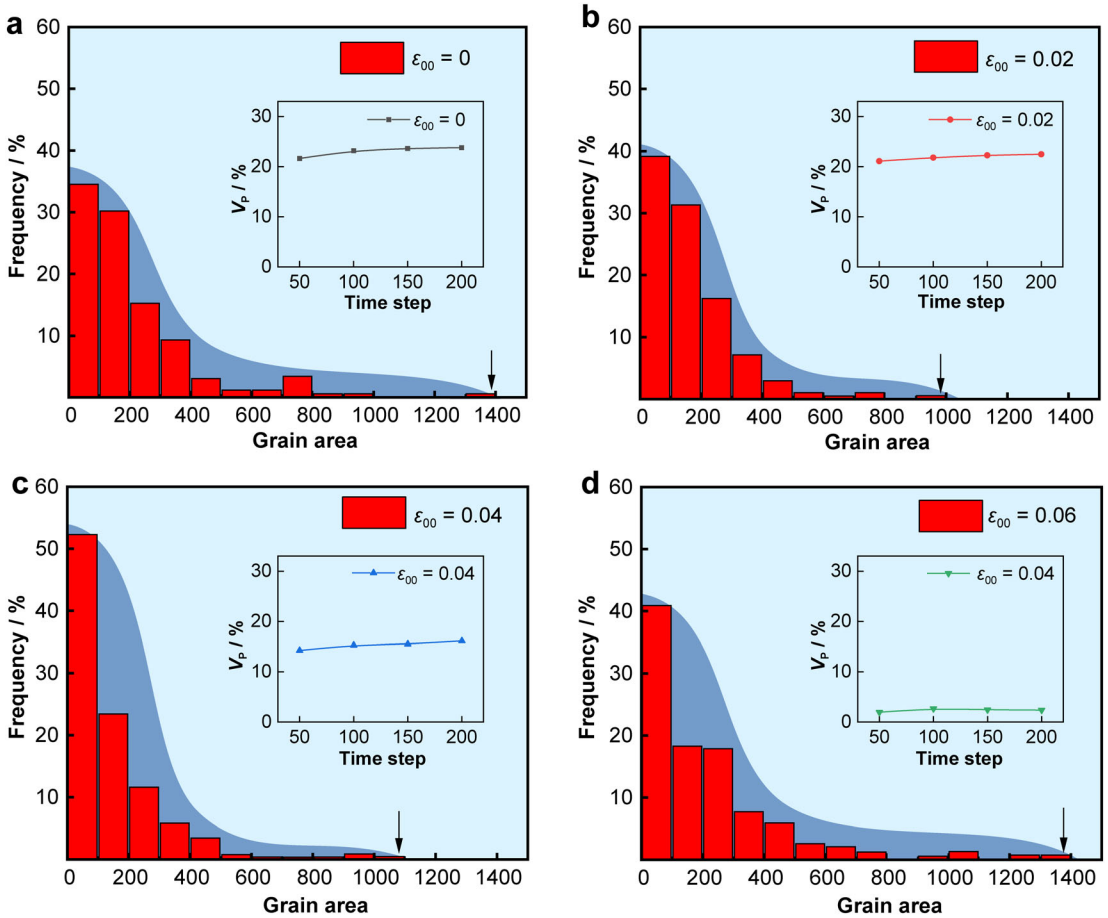

Fig. 3 Effect of lattice misfits **a** ε_{00} = 0, **b** ε_{00} = 0.02, **c** ε_{00} = 0.04 and **d** ε_{00} = 0.06 on grain area distribution in immiscible nanocrystalline alloys

The Gibbs free energy serves as an indicator of the thermodynamic potential of a system, and various mechanisms may be activated to minimize the total Gibbs free energy of a system. Among these mechanisms is the aggregation of solute atoms at GBs. Furthermore, precipitated phases can exhibit preferential nucleation at the GBs because these high-energy regions provide favorable sites for precipitate nucleation [46].

GB segregation is likely to occur when $\Omega_{gb} < 0$. For the concentration c_0 = 0.25, four sets of lattice misfits with values of ε_{00} = 0, 0.02, 0.04 and 0.06 were evaluated. In addition, the mixing enthalpy was set to a negative value of Ω_{gb} = −0.5. As shown in Fig. 4a–d, the red-colored areas in the figures correspond to precipitates that emerge from the blue matrix, while the yellow regions signify segregation. Furthermore, the segregation process undergoes gradual suppression as the lattice misfit rises from 0 to 0.06. This suppression is attributed to an inhibitory effect of the segregation process induced by elastic mismatch strain. Similarly, the microstructures of the systems with the lattice misfit of 0 and 0.02 are shown in Fig. 4a, b, respectively. Clearly, precipitation within the grains is significantly reduced when the lattice misfit increases to 0.02, with the precipitation primarily confined to GBs. However, when the lattice misfit further increases to 0.06, precipitation at GBs nearly disappears, resulting in the progressive accumulation of the solute at GBs.

Statistical analyses were performed to determine the grain area distribution of the nanocrystalline alloys at 200-time intervals and the time-dependent volume fraction of solute segregation (V_s) for different lattice misfits. As shown in Fig. 5, when the lattice misfit ε_{00} = 0, the volume fraction of solute segregation at the GBs in the system gradually decreased during the later stages of aging. This trend was mainly due to the enhanced precipitation of the second phase in the studied system, as the growth of the precipitated phase throughout the late aging period consumed some solutes from the matrix, resulting in a reduction in solute segregation at the GBs. When the lattice misfit increased to 0.02, the precipitation process was hindered, resulting in an increased solute volume fraction at the GBs. However, as the lattice misfit increased to 0.06,

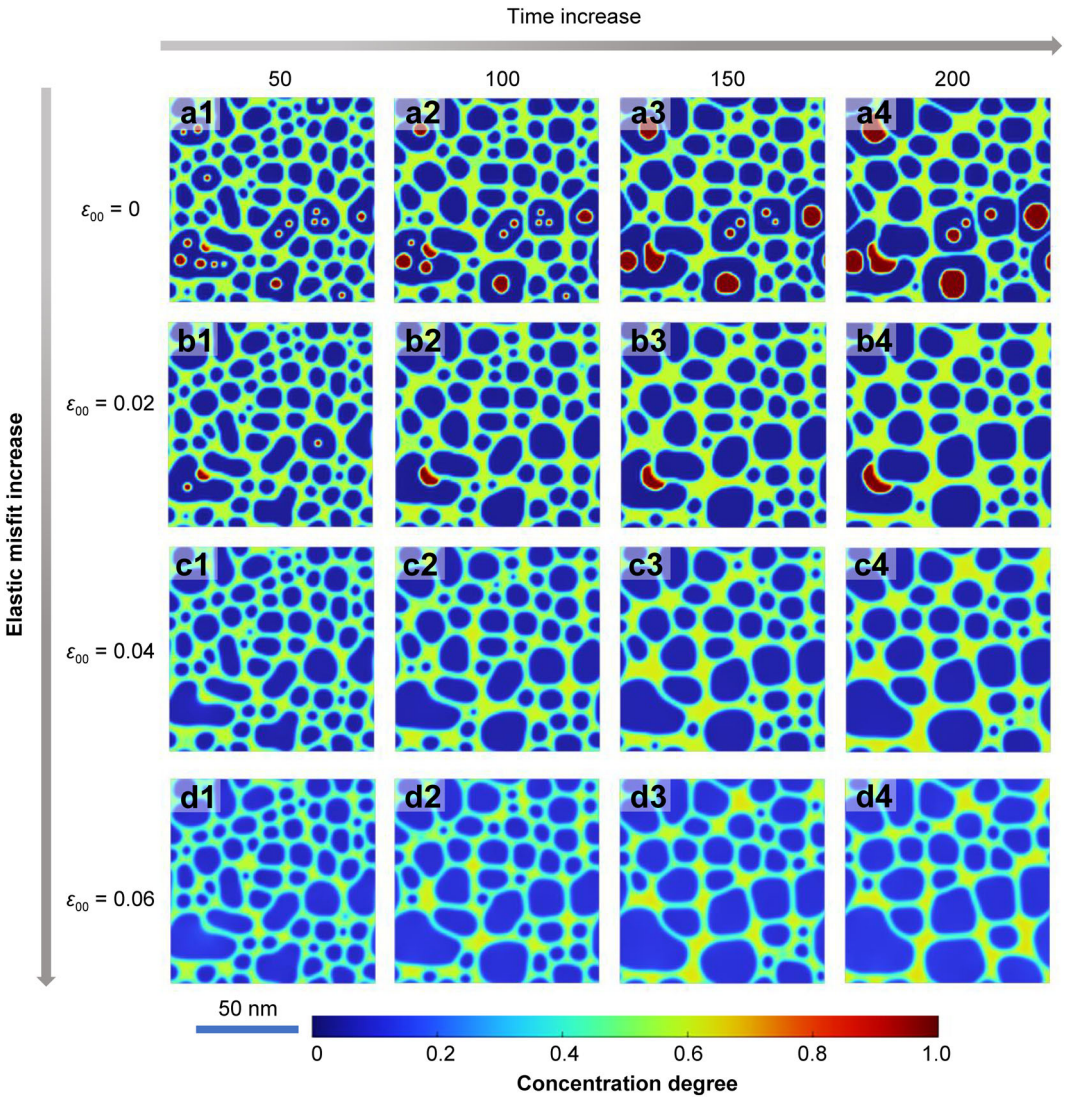

Fig. 4 Effect of lattice misfits **a** ε_{00} = 0, **b** ε_{00} = 0.02, **c** ε_{00} = 0.04 and **d** ε_{00} = 0.06 on microstructure evolution of GB segregation in miscible nanocrystalline alloys

it restricted the extent of solute segregation at the GBs. In comparison with the alloy system with a mismatch of 0.02, the volume fraction of solute segregation at the GBs in the system with a mismatch of 0.06 is substantially lower.

Moreover, for the nanocrystalline alloy system with a lattice misfit of 0, the grain area distribution ranged from 5 to 1162 nm^2. As the mismatch strain increased to 0.02, the maximum grain size of the alloy decreased significantly from 1162 to 766 nm^2. This reduction is attributed to the suppression of second-phase precipitation in the grains, primarily because of the relatively large elastic mismatch strain, which causes most solutes in the alloy to accumulate at the GBs, thereby impeding GB migration. As the lattice misfit continued to increase to 0.04, the grain size progressively expanded from 766 to 825 nm^2, which is due to the onset of elastic strain caused by the lattice mismatch. Ultimately, this strain completely halts the precipitation in miscible nanocrystalline alloys. At ε_{00} = 0.06, the solute segregation process within the system is also influenced by the elastic resistance. The inhibitory effect of solute segregation at the GBs on GB migration is weakened, resulting in a further increase in the maximum grain size to 1059 nm^2.

The simulation results suggest that introducing an elastic mismatch strain increases the nucleation barrier, thereby slowing the precipitation of the secondary phase inside the grains. Consequently, solute enrichment occurs in the GBs. Furthermore, precipitation at the GBs was suppressed as the mismatch strain increased. Ultimately, segregation in miscible nanocrystalline alloys is mitigated when the elastic mismatch strain reaches an excessively high value. This phenomenon not only weakens the pinning effect of

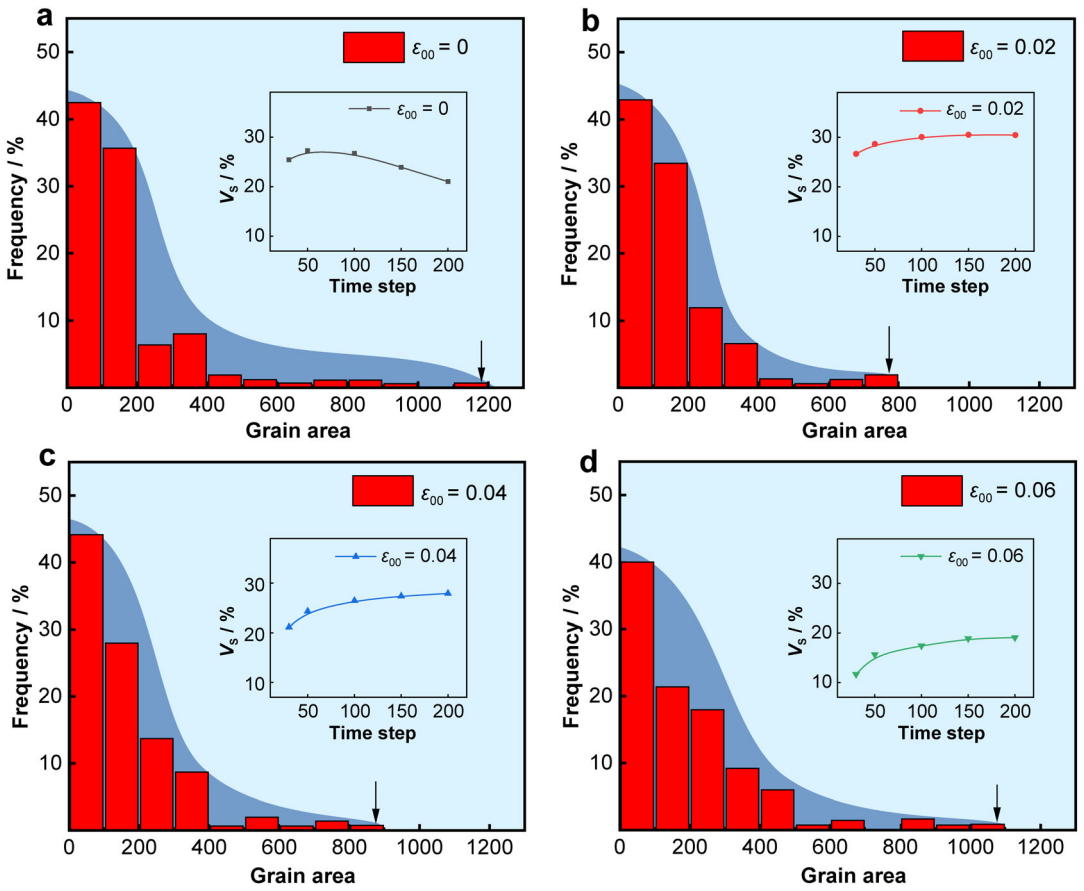

Fig. 5 Effect of lattice misfits **a** ε_{00} = 0, **b** ε_{00} = 0.02, **c** ε_{00} = 0.04 and **d** ε_{00} = 0.06 on grain area distribution of GB segregation in miscible nanocrystalline alloys

the second-phase precipitation at the GBs, but also inhibits solute segregation at the GBs. Consequently, accelerated grain growth occurred within the system.

3.3 Effect of mismatch strain on precipitation in immiscible nanocrystalline alloys

Referring to the free-energy derivation curves in Fig. 1, we studied four groups of solute concentrations to explore the interplay between the mismatch strain and composition, both within and beyond the spinodal decomposition domain. According to the aforementioned simulation results, the stabilization of grain sizes via solute segregation and second-phase pinning can be enhanced when ε_{00} = 0.02. Figure 6 shows the microstructure evolution of immiscible nanocrystalline alloys with ε_{00} = 0.02, Ω_{gb} = +0.5, and c_0 = 0.05, 0.10, 0.15 and 0.20, where the red-colored areas show the precipitates emerging from the blue matrix. No precipitation occurred in the system when c_0 = 0.05, and solute enrichment occurred at the three-phase junctions between several grains. When the solute composition increased to c_0 = 0.10, which lies within the spinodal decomposition region, a gradual emergence of second-phase precipitation was observed at the GBs.

The interfaces between the precipitates and grains consisted of incoherent boundaries without coherent strain, which subsequently induced a higher interfacial energy. Consequently, the propensity for second-phase precipitation along the GBs was notably higher than that within the bulk grains [15]. In such circumstances, second-phase precipitation exerted a substantial pinning effect on the GBs, thereby posing substantial challenges to GB migration and effectively preventing fast grain growth. As shown in Fig. 6b–d, the increase in solute concentration not only enhanced the solute enrichment process at the GBs, but also escalated the precipitation process.

Figure 7a–d displays the statistically calculated grain area distribution in immiscible nanocrystalline alloys, accounting for different compositions at 200-time steps. At a low solute composition of c_0 = 0.05, the grain area ranges from 4 to 1587 nm^2. Increasing the concentration from

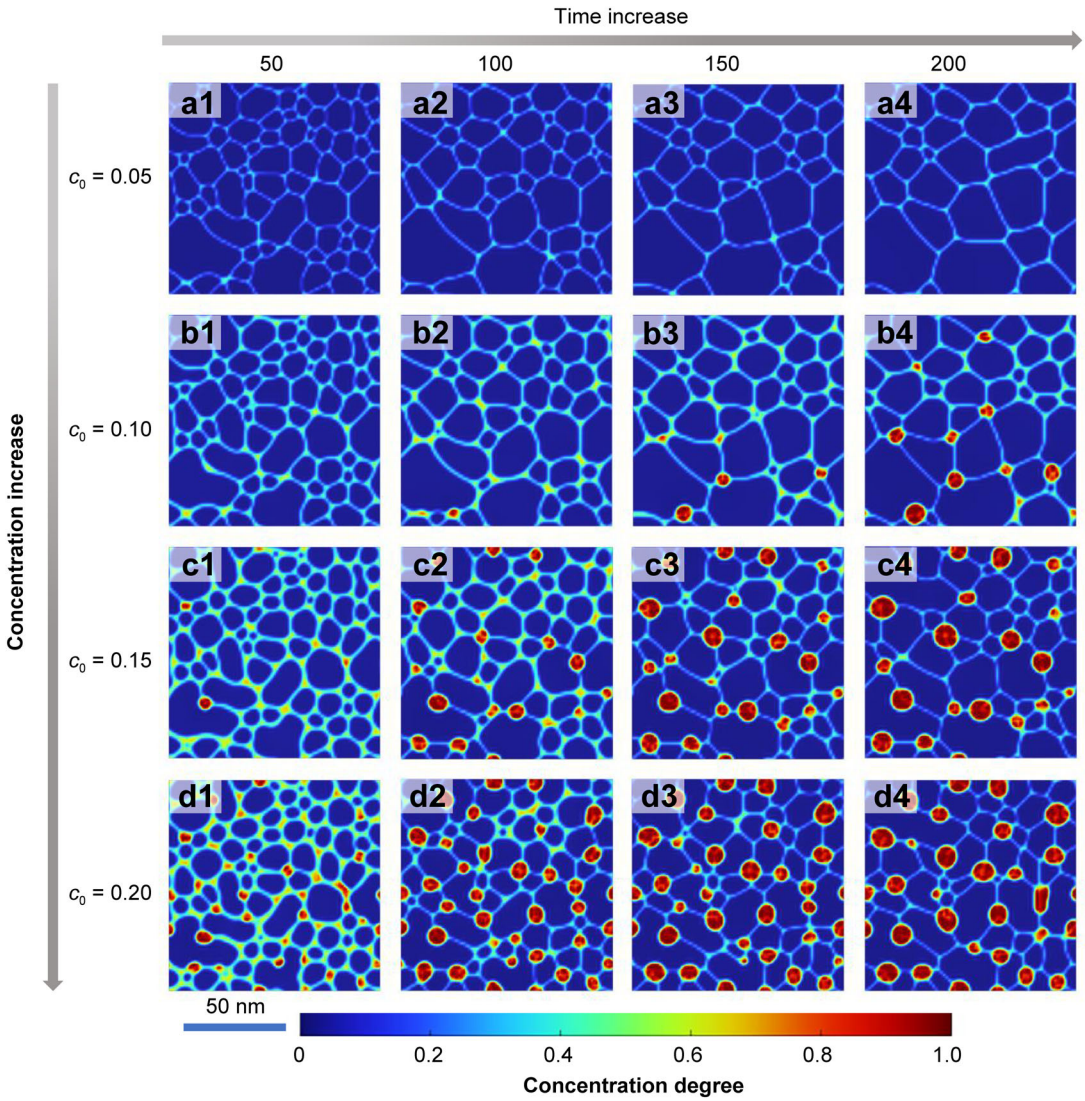

Fig. 6 Microstructure evolution of immiscible nanocrystalline alloys with **a** c_0 = 0.05, **b** c_0 = 0.10, **c** c_0 = 0.15, **d** c_0 = 0.20 and ε_{00} = 0.02

0.05 to 0.20 significantly decreases the maximum grain size from 1587 to 813 nm^2.

At time-step t = 200, the volume fraction of precipitation is ~4.6%, a value significantly lower than 10%. This finding suggests that the imposed elastic misfit strain inhibits the precipitation process within the system. For the solute composition of c_0 = 0.15 and 0.20, the volume fraction of precipitation increases from 11.2% to 16.9%, respectively. These fractions are significantly lower than the initial solute concentration because the elastic strain inhibits the precipitation of the second phase. This observation further demonstrates a decrease in grain area as the volume fraction of precipitate presents at GBs increases.

4 Conclusion

In this study, a phase-field model was constructed by incorporating the elastic mismatch strain and factors such as solute concentration and mixing enthalpy. The stabilization of the grain size via solute segregation and second-phase pinning can be enhanced by the appropriate coupling of the elastic misfit strain, thereby highlighting the existence of a critical threshold for the elastic mismatch. Furthermore, GB segregation is favored in nanocrystalline alloys with solute concentrations exceeding the spinodal decomposition domain, whereas precipitation at the GBs is preferred under other circumstances. Moreover, in

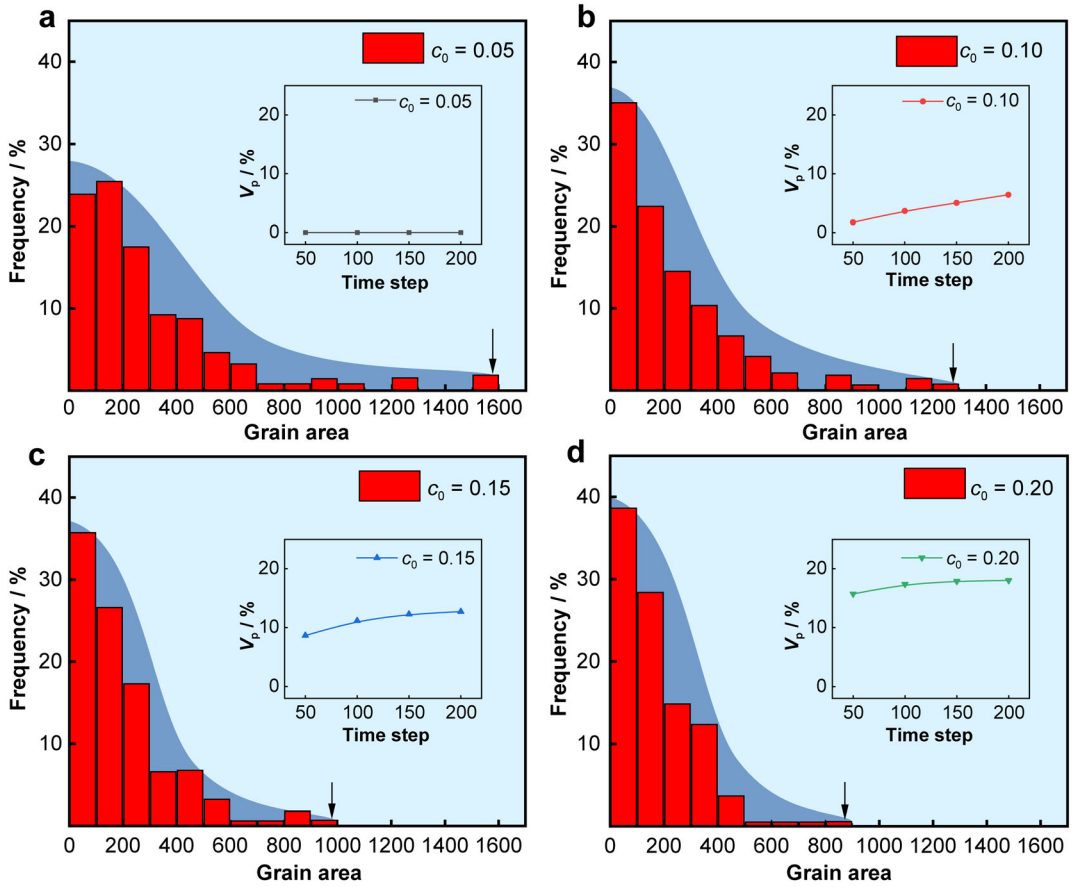

Fig. 7 Grain area distribution of immiscible nanocrystalline alloys with **a** c_0 = 0.05, **b** c_0 = 0.10, **c** c_0 = 0.15, **d** c_0 = 0.20 and ε_{00} = 0.02

immiscible nanocrystalline alloys with positive mixing enthalpies, most solutes tend to precipitate at the GBs, in contrast to miscible nanocrystalline alloys with negative mixing enthalpies, where solutes exhibit a preference for GB segregation. The findings of this study provide valuable insights for the design of nanocrystalline alloys with improved stability.

Acknowledgements This study was financially supported by the National Natural Science Foundation of China (Nos. 52122408, 51901013, 51971018, 52101188, 52225103, 52071023 and U20B2025), and the Funds for Creative Research Groups of NSFC (No. 51921001). H.H. Wu also thanks the financial support from the Fundamental Research Funds for the Central Universities (University of Science and Technology Beijing, Nos. FRF-TP-2021-04C1 and 06500135). The computing work was supported by the USTB Mat-Com of Beijing Advanced Innovation Center for Materials Genome Engineering.

Declarations

Conflict of interests The authors declare they have no conflicts of interest.

References

[1] Chookajorn T, Murdoch HA, Schuh CA. Design of stable nanocrystalline alloys. Science. 2012;337(6097):951. https://doi.org/10.1126/science.1224737.

[2] Gleiter H. Nanostructured materials: basic concepts and microstructure. Acta Mater. 2000;48(1):1. https://doi.org/10.1016/S1359-6454(99)00285-2.

[3] Meyers MA, Mishra A, Benson DJ. Mechanical properties of nanocrystalline materials. Prog Mater Sci. 2006;51(4):427. https://doi.org/10.1016/j.pmatsci.2005.08.003.

[4] Suryanarayana C, Koch CC. Nanocrystalline materials-current research and future directions. Hyperfine Interact. 2000;130(1/4):5. https://doi.org/10.1023/A:1011026900989.

[5] Zheng HB, Yan MY, An RY, Zhou XF, Feng T, Lan S. Nano-glass and applications in biomedicine. Chin J Rare Met. 2023;47(6):854. https://doi.org/10.13373/j.cnki.cjrm.XY22010019.

[6] Zhao XN, Fu DX, Wang LM, Guo ZM, Ban LQ, Gu T. Friction and wear properties of nano-Al_2O_3 dispersion strengthened copper with different yttrium contents. Chin J Rare Met. 2023;47(10):1460. https://doi.org/10.13373/j.cnki.cjrm.XY20100014.

[7] Ge JC, Liu AH, Wu ZD, Gu Y, Ke YB, Wang AD, Ren Y, Tang S, Ying HQ, Zhu H, Wang XL, Lan S. Phase transformation behavior of a dual-phase nanostructured Fe-Ni-B-Si-P-Nb metallic glass and its correlation with stress-impedance

properties. Rare Met. 2023;42(8):2757. https://doi.org/10.1007/s12598-023-02345-6.
[8] Wang JJ, Kou ZD, Fu S, Wu SS, Liu SN, Yan MY, Wang D, Lan S, Hahn H, Feng T. Microstructure and magnetic properties evolution of Al/CoCrFeNi nanocrystalline high-entropy alloy composite. Rare Met. 2022;41(6):2038. https://doi.org/10.1007/s12598-021-01931-w.
[9] Sanders PG, Eastman JA, Weertman JR. Elastic and tensile behavior of nanocrystalline copper and palladium. Acta Mater. 1997;45(10):4019. https://doi.org/10.1016/S1359-6454(97)00092-X.
[10] Belova IV, Murch GE. Diffusion in nanocrystalline materials. J Phys Chem Solids. 2003;64(5):873. https://doi.org/10.1016/s0022-3697(02)00421-3.
[11] Koch CC, Scattergood RO, Saber M, Kotan H. High temperature stabilization of nanocrystalline grain size: thermodynamic versus kinetic strategies. J Mater Res. 2013;28(13):1785. https://doi.org/10.1557/jmr.2012.429.
[12] Ding ZY, Gao JJ, Jiao ZB, Wu HH, Chen AY, Zhu J. Strain-magnetization property of Ni-Mn-Ga (Co, Cu) microwires. Rare Met. 2023;42(1):244. https://doi.org/10.1007/s12598-022-02071-5.
[13] Andrievski RA. Review stability of nanostructured materials. J Mater Sci. 2003;38(7):1367. https://doi.org/10.1023/a:1022988706296.
[14] Koch CC. Structural nanocrystalline materials: an overview. J Mater Sci. 2007;42(5):1403. https://doi.org/10.1007/s10853-006-0609-3.
[15] Gottstein G, Shvindlerman LS. Theory of grain boundary motion in the presence of mobile particles. Acta Metall Mater. 1993;41(11):3267. https://doi.org/10.1016/0956-7151(93)90056-x.
[16] Humphreys FJ, Hatherly M. Recrystallization and related annealing phenomena. Kidlington: Elsevier Science Ltd. 2004. 574. https://doi.org/10.1016/b978-0-08-044164-1.X5000-2.
[17] Palumbo G, Thorpe SJ, Aust KT. On the contribution of triple junctions to the structure and properties of nanocrystalline materials. Scr Metall Mater. 1990;24(7):1347. https://doi.org/10.1016/0956-716x(90)90354-j.
[18] Gao ZQ, Fultz B. Inter-dependence of grain growth, Nb segregation, and chemical ordering in Fe-Si-Nb nanocrystals. Nanostruct Mater. 1994;4(8):939. https://doi.org/10.1016/0965-9773(94)90100-7.
[19] Darling KA, Tschopp MA, VanLeeuwen BK, Atwater MA, Liu ZK. Mitigating grain growth in binary nanocrystalline alloys through solute selection based on thermodynamic stability maps. Comput Mater Sci. 2014;84:255. https://doi.org/10.1016/j.commatsci.2013.10.018.
[20] Saber M, Kotan H, Koch CC, Scattergood RO. Thermodynamic stabilization of nanocrystalline binary alloys. J Appl Phys. 2013;113(6):063515. https://doi.org/10.1063/1.4791704.
[21] Wang FY, Dong LS, Wu HH, Bai PH, Wang SZ, Wu GL, Gao JH, Zhu JM, Zhou XY, Mao XP. Enhanced nanocrystalline stability of BCC iron via copper segregation. Prog Nat Sci. 2023;33(2):185. https://doi.org/10.1016/j.pnsc.2023.05.001.
[22] Wang JJ, Wu SS, Fu S, Liu SN, Yan MY, Lai QQ, Lan S, Hahn H, Feng T. Ultrahigh hardness with exceptional thermal stability of a nanocrystalline CoCrFeNiMn high-entropy alloy prepared by inert gas condensation. Scr Mater. 2020;187:335. https://doi.org/10.1016/j.scriptamat.2020.06.042.
[23] Devaraj A, Wang W, Vemuri R, Kovarik L, Jiang X, Bowden M, Trelewicz JR, Mathaudhu S, Rohatgi A. Grain boundary segregation and intermetallic precipitation in coarsening resistant nanocrystalline aluminum alloys. Acta Mater. 2019;165:698. https://doi.org/10.1016/j.actamat.2018.09.038.
[24] Wu HH, Zhou XY, Li B, Wang SZ, Mao XP. Influence of C grain boundary segregation on high temperature mechanical properties of nanograined α-Fe. J. Iron Steel Res. 2021;33(4):315. https://doi.org/10.13228/j.boyuan.issn1001-0963.20210019.
[25] Wu HH, Dong LS, Wang SZ, Wu GL, Gao JH, Yang XS, Zhou XY, Mao XP. Local chemical ordering coordinated thermal stability of nanograined high-entropy alloys. Rare Met. 2023;42(5):1645. https://doi.org/10.1007/s12598-022-02194-9.
[26] Wang YB, Peng LM, Wu YJ, Zhao Y, Wang YX, Huang YB, Ding WJ. Phase-field modeling the effect of misfit on the precipitation of the second-phase particles and grain coarsening. Comput Mater Sci. 2015;100:166. https://doi.org/10.1016/j.commatsci.2014.10.066.
[27] Chakrabarti T, Manna S. Zener pinning through coherent precipitate: a phase-field study. Comput Mater Sci. 2018;154:84. https://doi.org/10.1016/j.commatsci.2018.07.041.
[28] Chen LQ. Phase-field models for microstructure evolution. Annu Rev Mater Res. 2002;32(1):113. https://doi.org/10.1146/annurev.matsci.32.112001.132041.
[29] Elder K, Gould H, Tobochnik J. Langevin simulations of nonequilibrium phenomena. Comput Phys. 1993;7(1):27. https://doi.org/10.1063/1.4823138.
[30] Lv SJ, Wu HH, Wang KY, Zhu JM, Wang SZ, Wu GL, Gao JH, Yang XS, Mao XP. The austenite to polygonal ferrite transformation in low-alloy steel: multi-phase-field simulation. J Mater Res Technol. 2023;24:9630. https://doi.org/10.1016/j.jmrt.2023.05.192.
[31] Wang KY, Lv SJ, Wu HH, Wu GL, Wang SZ, Gao JH, Zhu JM, Yang XS, Mao XP. Recent research progress on the phase-field model of microstructural evolution during metal solidification. Int J Minerals Metall Mater. 2023;30:2095. https://doi.org/10.1007/s12613-023-2710-x.
[32] Millett PC, Selvam RP, Saxena A. Stabilizing nanocrystalline materials with dopants. Acta Mater. 2007;55(7):2329. https://doi.org/10.1016/j.actamat.2006.11.028.
[33] Chen LQ, Yang W. Computer simulation of the domain dynamics of a quenched system with a large number of nonconserved order parameters: the grain-growth kinetics. Phys Rev B Condens Matter. 1994;50(21):15752. https://doi.org/10.1103/physrevb.50.15752.
[34] Abdeljawad F, Foiles SM. Stabilization of nanocrystalline alloys via grain boundary segregation: a diffuse interface model. Acta Mater. 2015;101:159. https://doi.org/10.1016/j.actamat.2015.07.058.
[35] Abdeljawad F, Lu P, Argibay N, Clark BG, Boyce BL, Foiles SM. Grain boundary segregation in immiscible nanocrystalline alloys. Acta Mater. 2017;126:528. https://doi.org/10.1016/j.actamat.2016.12.036.
[36] Ganguly J. Thermodynamic modelling of solid solutions. EMU Notes Mineral. 2001. https://doi.org/10.1180/EMU-notes.3.3.
[37] Johnson AE, Voorhees PW. A phase-field model for grain growth with trijunction drag. Acta Mater. 2014;67:134. https://doi.org/10.1016/j.actamat.2013.12.012.
[38] Hu SY, Chen LQ. A phase-field model for evolving microstructures with strong elastic inhomogeneity. Acta Mater. 2001;49(11):1879. https://doi.org/10.1016/S1359-6454(01)00118-5.
[39] Khachaturyan AG, Semenovskaya S, Tsakalakos T. Elastic strain energy of inhomogeneous solids. Phys Rev B Condens Matter. 1995;52(22):15909. https://doi.org/10.1103/physrevb.52.15909.
[40] Li JL, Li Z, Wang Q, Dong C, Liaw PK. Phase-field simulation of coherent BCC/B2 microstructures in high entropy alloys. Acta Mater. 2020;197:10. https://doi.org/10.1016/j.actamat.2020.07.030.
[41] Li YS, Zhu H, Zhang L, Cheng XL. Phase decomposition and morphology characteristic in thermal aging Fe-Cr alloys under applied strain: a phase-field simulation. J Nucl Mater. 2012;429(1–3):13. https://doi.org/10.1016/j.jnucmat.2012.05.026.
[42] Cahn JW, Hilliard JE. Free energy of a nonuniform system. III. Nucleation in a two-component incompressible fluid. J Chem Phys. 1959;31(3):688. https://doi.org/10.1063/1.1730447.
[43] Wang YH, Zhang ZW, Pi ZP, Lin JG, Wen C. Phase field simulation of spinodal decomposition in Zr–Nb alloys for

implant materials. J. Appl. Phys. 2019;126(8). https://doi.org/10.1063/1.5096820.
[44] Abinandanan TA, Haider F. An extended Cahn-Hilliard model for interfaces with cubic anisotropy. Philos Mag A. 2001;81(10):2457.
[45] Moelans N, Blanpain B, Wollants P. An introduction to phase-field modeling of microstructure evolution. Calphad. 2008;32(2):268. https://doi.org/10.1016/j.calphad.2007.11.003.
[46] Semboshi S, Sato M, Kaneno Y, Iwase A, Takasugi T. Grain boundary character dependence on nucleation of discontinuous precipitates in Cu-Ti alloys. Materials. 2017;10(4):415. https://doi.org/10.3390/ma10040415.